High-resolution study of ion-induced $K\alpha_{1,2}$ x-ray spectra from high-Z elements

D. F. Anagnostopoulos,* G. Borchert, and D. Gotta
Institut für Kernphysik, Forschungszentrum Jülich, D-52425 Jülich, Germany

K. Rashid
Department of Mathematics, Quaid-i-Azam University, Islamabad, Pakistan

D. H. Jakubassa-Amundsen
Physics Section, University of Munich, Am Coulombwall 1, D-85748 Garching, Germany

P. A. Amundsen
Institute for Mathematics and Natural Science, University Center in Rogaland, N-4004 Stavanger, Norway
(Received 17 February 1998)

The $K\alpha_{1,2}$ x rays emitted from La, Tb, Ta, and U targets induced by proton nitrogen, and neon ion bombardment at incident energies between 15 and 28 MeV/nucleon have been measured with a high-resolution crystal spectrometer. The spectra reflect the decay of a K vacancy in the presence of multiple $L, M, N, \ldots$ shell ''spectator'' vacancies. The L-shell ionization probabilities for impact parameters in the interior of the target's K shell are extracted from the measured spectra and compared with extensive theoretical calculations of ionization probabilities, based on the semiclassical separate-atom perturbation theory [semiclassical approximation (SCA)]. The projectile velocity varies from 60% to 125% of the target L electron velocity, so we can compare experimental data with theoretical predictions as a function of the relative velocity. We find that wave-function effects play an important role for an accurate calculation of the ionization probability. The experimental results agree well with the SCA predictions when Hartree-Fock-type wave functions are used [variationally determined optimized potential (SCA-OPM)]. Relativistic hydrogenic wave functions (SCA-HYD) provide a reliable description of experimental data only in the case of the uranium target. The influence of electron capture and intrashell coupling is also calculated and discussed. An independent comparison of theoretical constructed spectra with the experimental ones confirms the validity of the SCA-OPM. The hole-hole angular momentum coupling between ''active'' and ''spectator'' holes has been observed as predicted. [S1050-2947(98)05609-1]

PACS number(s): 34.50.Fa, 32.30.Rj, 32.70.−n, 34.10.+x

I. INTRODUCTION

The study of multiple ionization of inner- and outer-shell electrons in heavy ion-atom collisions is a challenging field of continuing interest both experimentally and theoretically. The phenomena of inner-shell ionization form the basis of trace element analysis, ion implantation studies, stripping of heavy projectiles when passing through matter, and other related applications [1,2].

The presence of multiple vacancies in inner and outer shells leads to a complex structure of the $K\alpha$ x-ray spectrum. It consists of the diagram line, which originates from a transition in a state with a single K-shell vacancy, and the satellite structure, which originates from K transitions in multiply ionized states. Since inner-shell vacancies reduce the screening of the nuclear charge, the satellite lines (usually) are shifted towards the high-energy side of the diagram line. The energy shift for the K transition in the presence of L spectator holes is large enough that these lines appear separated from the diagram line, and therefore it is possible to study them with high-resolution x-ray spectroscopy (a survey of high-resolution particle-induced x-ray emission instrumentation is given by [3]).

The study of the complex K x-ray spectra provides an efficient way to probe the atom at an early stage after the collision, and to gain information on inner-shell vacancy production as well as on the rearrangement of vacancies due to the various electronic relaxation processes taking place during the short lifetime of a K hole. This allows basic and applied research studies. As an example, a significant improvement in elemental analytical application has been obtained, where the high resolution helps to detect minor elements otherwise remaining undetected [4,5]. Moreover, as the structure of satellite lines is highly sensitive to differences in chemical bonding up to the third row in the Periodical Table, they are extensively used for chemical state characterization on solid materials [6,7].

However, the presence of bonding effects may obscure the comparison between experimentally extracted ionization probabilities and theoretical predictions, which are mostly based on atomic model calculations. This obstacle can be overcome using high-Z elements, as in this case the L-shell electrons are deep inside the target atom and thus are not influenced by the valence electrons.

The high-resolution measurement of K x-ray transitions from intermediate to high-Z elements requires crystal spectrometers in transmission geometry, installed at an accelerator facility. During the past decade, these types of high-

*Electronic address: danagno@nrt.cs.uoi.gr

resolution systematic studies were initiated at Paul Scherrer Institute in Villigen [8–12], where middle-light collision systems were investigated, whereas the study of medium-heavy to heavy elements was performed at the Institut für Kernphysik, Forschungszentrum Jülich [13–15].

The present study has been performed with the high-energy beam of the Jülich cyclotron and the KVI cyclotron, in Groningen [16]. The colliding systems have been chosen in such a way that the projectile velocities are of the order of the L electron Bohr velocities of the target atoms. We focus our attention on the L spectator hole satellite structure of the $K\alpha$ x-ray transitions. The mean L-shell ionization probabilities are extracted directly from the experimental spectra, describing the multiple ionization cross sections by a binomial distribution of the single electron ionization probabilities, based on the assumption of the independent electron ionization. The rearrangement of the created vacancies during the lifetime of the K hole through radiative, Auger, and Coster-Kronig transitions, and the energy shifts of the K x rays due to the presence of vacancies, are taken into account. The reliability of theoretical predictions is checked, as a function of the ratio between target electron velocity and projectile velocity. The direct ionization cross sections have been calculated within various perturbative approaches in the framework of the semiclassical approximation (SCA). The effects of subshell coupling and electron transfer have also been considered. From these models we have constructed theoretical spectra, which are then compared with the experimental results. In order to construct the theoretical spectra, knowledge of the ionization cross sections, the multiple ionization cross sections, the rearrangement of the inner vacancies, and the transition energies is required.

The paper is organized as follows. Section II describes the experimental setup and Sec. III outlines the calculations of the ionization probabilities. The structure of the experimental spectra is described in Sec. IV and the results are presented in Sec. V, followed by the summary (Sec. VI). Atomic units ($\hbar = m = e = 1$) are used unless otherwise indicated.

II. EXPERIMENTAL SETUP

The energy difference between a $K\alpha_1 L^1$ satellite transition ($K\alpha_1$ transition in the presence of one L spectator hole) and the diagram $K\alpha_1$ transition for middle to heavy elements is typically of the order of the natural linewidth (see Sec. IV A). Solid-state detectors cannot resolve these satellites but this is possible with a high-resolution crystal spectrometer.

Thus a DuMond-type focusing crystal spectrometer was used to analyze the photon energies (Fig. 1) [17]. A cylindrically bent quartz crystal with a radius of curvature of $R = 464$ cm has been used with lattice planes (110) having a lattice constant of ≈ 2.5 Å. The crystal dimensions were $100 \times 100 \times 4\ \text{mm}^3$ and the effective aperture was $50 \times 50\ \text{mm}^2$. The distance between the crystal and the target is $R \cos\theta$ (for a discussion on the geometry of curved crystal spectrometers in transmission geometry, see Ref. [18]). The Bragg angle θ is measured by an interferometric angle measuring system. The crystal is moved in steps across the range of reflection angle with a minimal step size of 0.2 arc sec and a reproducibility of 0.01 arc sec, which is made possible by a piezoceramic stabilization unit.

After reflection from the lattice planes, the photons pass a Soller slit collimator of 1 m length having a transmission of about 60%. A high-purity Ge detector with an active size of 60 mm diameter and an effective thickness of 12 mm is placed behind the collimator to detect the x rays. For background suppression, the detector is enclosed in a lead container with 10 cm thick walls.

The collimator-detector system rotates with twice the Bragg angle around the rotation axis of the crystal. This movement is controlled and regulated by an optical device with an accuracy of about 5 arc sec. The spectrometer is able to measure at a positive and negative angle within a range of $\pm 5°$ [17]. Measuring at both angles reduces to a large extent the systematic errors originating from a skew line shape, temperature drift, and source movements.

The isochronous cyclotrons at Forschungszentrum Jülich and KVI Groningen, in combination with electron cyclotron resonance (ECR) sources, supply the projectiles (p to Ne) in an energy range of 15–45 MeV/nucleon and with currents in the order of hundreds of nA. The spectrometer was installed at external beamlines. The beam hits the target material in a special chamber. The targets were thin metal foils of size $3 \times 20 \times 0.1\ \text{mm}^3$ mounted in a graphite holder to minimize background production. The holder was connected to a cooling system to conduct away the heat produced by the intense beam in the target. The target could be rotated around a vertical axis as well as tilted by a remote motor control. These movements enabled the minimization of the effective target size as seen by the spectrometer. The angle between the photon detection direction and the target's surface was less than 2° while the angle between the beam direction and the target surface was about 70°. This geometrical arrangement in conjunction with the self-absorption of the emitted x-ray photons determined the projectile's effective penetration depth to be less than 10 μm. The projectile's energy loss over this depth is less than 3% and consequently its energy is considered constant within the effective target thickness. The produced x-ray radiation penetrated a 2 m long lead collimator. A movement of the reaction chamber in this direction via remote control allowed the fine adjustment of the focal length for each Bragg angle. To monitor the beam intensity at the target, a second Ge detector was installed close to the crystal, which sees the target area under conditions similar to those of the crystal.

The signals from the main detector and the monitor detector were treated in an identical way (Fig. 1). After amplification and filtering by a timing single-channel analyzer (TSCA) they were fed into two branches. The signals in the ''slow'' branch were fed into CAMAC analog-to-digital converters (ADC). The signals in the ''fast'' branch were analyzed in a logical network. After suppression of saturated pulses, the output signal gates the ADC and is registered in fast counters for a quick control of the experimental setting. For each measured point, the position, measuring time, and the pulse height spectra of the main detector and monitor detector were stored by a PDP 24/11 computer. The PDP computer performed also the control of the measurement procedure and parameters and allowed an automatic operation for the following: (i) positioning of the spectrometer at a preselected angle, (ii) start of the measurement when the

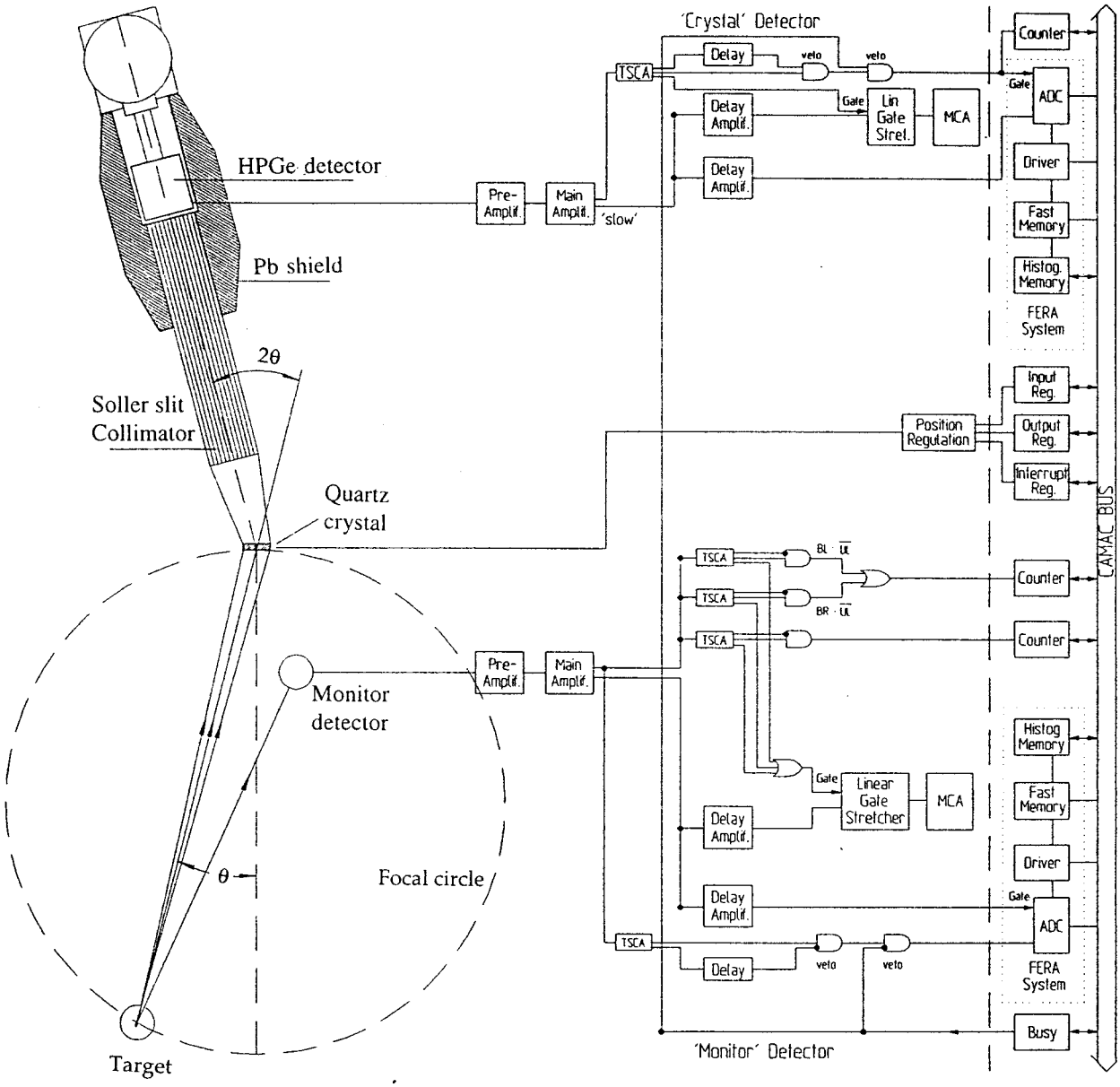

FIG. 1. Jülich focusing DuMond crystal spectrometer with the main components and the block diagram of the electronics circuitry.

whole system is in the correct position, (iii) stop of the measurement after a preselected time or when a fault is detected, and (iv) storing of the data and to repeat steps (i)–(iv) until interrupted manually.

The spectrometer was adjusted and calibrated with the γ and x rays. Since γ rays have negligible natural widths, we used them to adjust the target position and to measure the spectrometer response function. Thin radioactive foils with a thickness less than 0.1 mm were placed at the target position and adjusted to minimize the geometrical linewidth. Adjustment of focal length and energy calibration was carried out by measuring several γ lines in different orders of reflections. Using ^{169}Yb and ^{170}Yb γ radioactive sources we find that the crystal response function is described well by a Gaussian with a full width at half maximum (FWHM) of about 4.5 arc sec for 60–90 keV photon energies.

The on-line adjustment is made by measuring the x rays from bombardment of the foil target with a proton beam. The intensity distribution from the target using the proton beam is very similar to that of the heavy ion beam, but the x-ray spectra show no satellite structure (see Sec. IV). Therefore, the line shapes are used to model the fit profiles, to check the energy dispersion and resolution, and to estimate the geometrical target width. By using Voigt profiles, originating from the convolution of a Gauss function with a Lorentzian, we obtained a reduced χ^2 around unity, which confirms that this straightforward approach describes the experimental data well. The extracted Lorentzian widths are in good agreement with the natural widths of the corresponding $K\alpha_{1,2}$ x-ray transitions as given by [19] and [20].

The energy dispersion of the spectrometer was checked comparing the energy differences between the measured diagram lines and the energy differences using the experimental data from [21] and the theoretical values using the MCDF

TABLE I. Reduced velocity η_L is defined as the ratio of the projectile impact velocity and the velocity of the *L*-shell target electrons. The impact parameter for which the *K*-shell ionization probability has dropped by two orders of magnitude from the value corresponding to the impact parameter $b=0$ is $b_{\max}$, $\overline{b_K}$ gives the mean impact parameter for *K*-shell ionization, and $\langle r_K\rangle$ and $1/\langle r_K^{-1}\rangle$ are the Dirac-Hartree-Fock calculated mean radius and the inverse of the mean inverse radius of the target *K*-shell electrons.

System	η_L	$b_{\max}$ (fm)	$\overline{b_K}$ (fm)	$\langle r_K\rangle$ (fm)	$1/\langle r_K^{-1}\rangle$ (fm)
403-MeV $N^{7+}\rightarrow$La	1.24	2700	650	1328	854
350-MeV $N^{7+}\rightarrow$Ta	0.84	2000	400	988	617
500-MeV $Ne^{10+}\rightarrow$Ta	0.84	2000	400	988	617
210-MeV $N^{7+}\rightarrow$Tb	0.75	2000	460	1136	722
300-MeV $Ne^{10+}\rightarrow$Tb	0.75	2000	460	1136	722
500-MeV $Ne^{10+}\rightarrow$U	0.61	1200	250	723	430

code [22]. The agreement is very good. As a typical example, for the La $K\alpha$ fine-structure energy difference $(E_{K\alpha_1}-E_{K\alpha_2})$, we measured (406.5 ± 0.5) eV compared with (407.7 ± 0.3) eV given by [21] and 408.4 eV using the MCDF code [23].

III. IONIZATION PROBABILITIES

At the projectile energies around 15–28 MeV/nucleon, the collision time (10^{-20} sec) is much shorter than the decay time (10^{-17}–10^{-18} sec) of the *K* hole. Therefore, the creation and subsequent decay of the vacancies can be treated as separate processes, and the dynamics of the excitation process is sufficiently well described in terms of ionization of one or more independent electronic states, induced by the time-dependent projectile field. So first of all, calculations for the production of single vacancies, caused by direct ionization, are needed. We will now give an outline of these calculations.

A. Direct ionization in first-order perturbation theory (SCA)

In the semiclassical approximation (SCA) [24], the probability for exciting a target electron from the bound state Ψ_i (with energy E_i) to a continuum target state Ψ_f (with energy E_f and angular momentum quantum numbers j_f, l_f, m_f) is given by [25,26]

$$p_i^{\mathrm{SCA}}(b)=\int_0^\infty dE_f \sum_{j_f l_f m_f} |a_{fi}|^2 \tag{3.1}$$

with

$$a_{fi}=-i\int_{-\infty}^{+\infty} dt\ e^{i(E_f-E_i)t}\langle \psi_f|V_p+V_R|\psi_i\rangle, \tag{3.2}$$

where b is the impact parameter, and the perturbing potential is composed of the electron-projectile field

$$V_p=-\frac{Z_p}{|\vec{R}(t)-\vec{r}|} \tag{3.3a}$$

and the recoil field

$$V_R=-\frac{\mu}{M_T}(1-\delta m)\vec{r}\cdot\ddot{\vec{R}}. \tag{3.3b}$$

$\vec{R}(t)$ and $\vec{r}$ are the internuclear and electronic coordinate, Z_P is the projectile nuclear charge, μ is the reduced mass of the projectile-target system, M_T is the target mass, and δm is a relativistic mass correction [27].

The proper choice of wave functions is sensitive to the reduced velocity, η, defined as the ratio of the projectile impact velocity, v, to the target electron velocity, v_{el}. For impact velocities in the order of the electron Bohr velocity in the shell under consideration, the use of relativistic hydrogenic wave functions for the multielectron target no longer gives a satisfactory description of the subshell ionization probabilities. Hence the wave functions are calculated from a variationally determined optimized potential [28]. This potential yields results that are as accurate as those obtained from Dirac-Fock-Slater potentials [29]. For high collision energies ($\eta>1$), the results for the ionization probability $P(b)$ obtained from this potential may easily exceed the results for hydrogenic wave functions, especially at small impact parameters [15,25]. For the systems investigated here, this is particularly true for the *M* shell (and higher shells), and to a lesser extent also for the *L* shell. For the *K* shell, on the other hand, the ratio between the collision velocity and the Bohr velocity is only about one-half. In this case the nonhydrogenic effects are small for the *K* shell.

The electron velocities v_{el} have been calculated from their kinetic energies, E_{kin}, as $v_{\mathrm{el}}=\sqrt{(1+E_{\mathrm{kin}}/mc^2)^2-1}c$. The kinetic energies are taken from the tabulated values of [30]. The velocity of the targets' *L*-shell electrons has been estimated as a statistical average over the electrons' velocities of the individual *L* subshells (an *L*-shell velocity as average over the *L* subshells weighted according to the ionization probabilities differs by less than 1% from the statistical average). The reduced velocities η_L obtained for the various studied collision systems are given in Table I.

Examining as a typical case the 403-MeV $N^{7+}\rightarrow$La system, the direct ionization probabilities, for the *K* and L_{III} subshell, as a function of the impact parameter *b*, calculated in the framework of SCA using several sets of wave functions, are shown in Fig. 2. For the *K*-shell ionization the two different wave-function sets give comparable results (projectile velocity is about 55% of the lanthanum *K*-shell electrons' velocity), but the prediction of the Dirac-Fock-type potential and the screened hydrogenic potential differ almost by a factor of 2 for the *L*-shell ionization (projectile velocity is about the velocity of the *L*-shell electrons) and differs by a factor

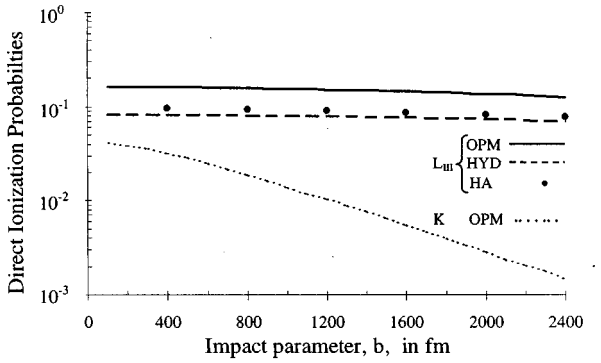

FIG. 2. Direct electron ionization probabilities $P^{\mathrm{SCA}}(b)$ as a function of the impact parameter b from the K and L_{III} subshell of a lanthanum atom during its bombardment with 403-MeV N^{7+}, according to the semiclassical approximation (SCA). The L_{III} ionization probabilities have been calculated using the OPM wave functions (SCA-OPM), relativistic screened hydrogenic (SCA-HYD), and the tabulated values of Hansteen *et al.* [31] based on screened hydrogenic wave functions (SCA-HA). The K probabilities have been calculated by using the SCA-OPM.

of 4 for the M shell (projectile velocity is about four times larger than the velocity of the M-shell electrons, $\eta_M=4$) [15].

On the other hand, the use of separate atom wave functions may be questioned for the K shell. However, because our systems have a strong asymmetry ($Z_P/Z_T \ll 1$, with Z_T the target nuclear charge), the molecular effects are small and the separate atom perturbation theory provides reliable results. Since the excitation energy for a K-shell electron is much larger than for the higher shells, and consequently also the minimum momentum transferred to the electron, $q_{\min}=(E_f-E_i)/v$, the impact-parameter distribution of the K-shell ionization probability is much steeper than for the L and M shells (Fig. 2). If one defines $b_{\max}$ as the impact parameter for which the K-shell ionization probability has dropped by two orders of magnitude (Table I), the ionization probabilities for the L and M shells are nearly constant in the impact parameter region $b<b_{\max}$ [13–15].

The mean impact parameter b_K for the K-shell electron ionization is given by

$$\bar{b}_K=\frac{\int_0^\infty db\ bP_k(b)}{\int_0^\infty db\ P_k(b)}\approx\frac{\int_0^{b_{\max}} db\ bP_k(b)}{\int_0^{b_{\max}} db\ P_k(b)}. \tag{3.4}$$

The K-shell electron ionization takes place predominately in the interior of the mean K-shell target-atom radius, r_K, for the collision systems considered here.

The K-, L-, and M-subshell probabilities per target electron, at $b=0$, calculated with a straight-line path for the internuclear motion (such that $V_R=0$) and with relativistic wave functions from an optimized target potential, are listed in Table II. The L- and M-shell binding energies in the presence of a K vacancy have been obtained with the multiconfiguration Dirac-Fock code of Desclaux [22]. The subshell-ionization probabilities are obtained by multiplying the tabulated values by the subshell occupation number.

In Table III we show the ratio T_n of the SCA L-shell ionization probability with optimized potential wave functions (SCA-OPM) to hydrogenic wave functions (SCA-HYD), for $b=0$. The latter was obtained from the coupled-subshell code (Sec. III B) by setting the coupling matrix element M_{nk} equal to zero. The deviation of T_n from unity is mainly attributed to the difference in the optimized and the hydrogenic potentials, and to a much lesser extent to the different number of partial waves included in the expansion of the transition matrix elements ($l\leqslant 6$ for the SCA-OPM and $l\leqslant 2$ for the SCA-HYD). From Table III it follows that T_n increases with reduced velocity up to nearly a factor of 2 for the fastest and lightest collision system investigated.

B. *L*-shell ionization in the coupled subshell approximation (CSA)

For small energy spacing between adjacent subshells, the rearrangement of vacancies among the subshells during the course of the collision becomes important [32]. This coupling effect is the more pronounced the lower the collision velocities and the stronger the interaction V_P with the projectile. Disregarding any couplings to other shells, the solution to the exact two-center Hamiltonian for the active electron is expanded as

$$\psi(t)=\sum_n a_n(t)|\psi_n\rangle+\sum_f \int a_f(t)|\psi_f\rangle, \tag{3.5a}$$

where the first sum runs over all subshell states ψ_n of the shell under consideration, and ψ_f are the continuum target eigenstates. For very asymmetric collisions where the total L-shell ionization probability is well reproduced by first-order perturbation theory, it is sufficient to treat the coupling to the continuum in perturbation theory. With this approxi-

TABLE II. (Sub)shell direct ionization probability $P^{\mathrm{SCA\text{-}OPM}}$, in percent, per target electron, according to the SCA theory, for impact parameter $b=0$. The target wave functions are calculated using optimized potentials (OPM).

System	Direct ionization probability, $P^{\mathrm{SCA\text{-}OPM}}$ $(b=0)$ (%)								
	K	L_{I}	L_{II}	L_{III}	M_{I}	M_{II}	M_{III}	M_{IV}	M_{V}
403-MeV $N^{7+}\rightarrow$La	2.10	2.49	4.28	4.06	2.66	4.17	4.11	4.39	4.34
350-MeV $N^{7+}\rightarrow$Ta	1.05	1.66	3.65	3.47	2.60	3.88	4.07	4.91	4.83
500-MeV $Ne^{10+}\rightarrow$Ta	2.15	3.38	7.46	7.07	5.31	8.05	8.30	10.00	9.86
210-MeV $N^{7+}\rightarrow$Tb	1.00	2.07	4.88	4.79	4.17	5.93	6.28	8.32	8.26
300-MeV $Ne^{10+}\rightarrow$Tb	1.97	4.24	9.98	9.81	8.77	12.30	12.90	17.50	17.40
500-MeV $Ne^{10+}\rightarrow$U	1.18	2.55	4.71	4.31	4.80	5.35	5.77	8.55	8.43

TABLE III. Ratio T_n of L-subshell ionization probabilities calculated using optimized-potential wave functions (SCA-OPM) to hydrogenic wave functions (SCA-HYD), respectively, for impact parameter $b=0$.

System	T_n		
	L_{I}	L_{II}	L_{III}
403-MeV $N^{7+}\rightarrow$La	1.40	1.70	1.78
350-MeV $N^{7+}\rightarrow$Ta	1.30	1.49	1.60
500-MeV $Ne^{10+}\rightarrow$Ta	1.31	1.48	1.59
210-MeV $N^{7+}\rightarrow$Tb	1.20	1.41	1.51
300-MeV $Ne^{10+}\rightarrow$Tb	1.20	1.40	1.50
500-MeV $Ne^{10+}\rightarrow$U	1.24	1.21	1.30

mation the expansion coefficients a_n and a_f satisfy the following system of coupled differential equations [33]:

$$\dot{a}_n = -ia_nE_n - i\sum_k a_kM_{nk} - iM_{nf}e^{-iE_ft} \qquad (3.5b)$$

with boundary conditions of an initial vacancy in the continuum state f ($a_f=1$) and a_n ($t\rightarrow-\infty$)$=0$. The sum index k runs over all (bound) subshell states and E_n are their energies. The probability for ionizing the subshell n (i.e., for finding a vacancy in the state n) is obtained from

$$P_n^{\mathrm{CSA}}(b) = \tfrac{1}{2}\int_0^\infty dE_f \sum_{j_f l_f}\sum_{m_f>0}[|a_n^{(+)}(t\rightarrow\infty)|^2 + |a_n^{(-)}(t\rightarrow\infty)|^2], \qquad (3.6)$$

where $a_n^{(\pm)}$ is obtained from a linear combination of the subshell states with positive and negative magnetic quantum numbers [33]. From this expression the perturbation result given by Eq. (3.1) is easily recovered by setting the coupling matrix element M_{nk} equal to zero and by making a phase transformation $a_{fn}\equiv a_ne^{iE_nt}$.

This approach has been applied to the calculation of L-subshell ionization probabilities for our collision systems. For the sake of simplicity, relativistic hydrogenic wave functions have been used, with an effective target charge $Z_{\mathrm{eff}} = n\langle r^{-1}\rangle/\sqrt{n^{-2}+\langle r^{-1}\rangle^2/c^2}$. Here, $\langle r^{-1}\rangle$ is the mean value of the inverse shell radius of the state n with the maximum angular momentum j. The shell radii and the subshell energies have been calculated with the Desclaux code [22]. In Table IV the ratio of the subshell ionization probability with and without the inclusion of the intrashell coupling is listed for an internuclear Coulomb trajectory.

The use of more accurate wave functions in the CSA calculations would lead to a much more complicated numerical code. Assuming, however, that the ratio R_n of the subshell coupling probabilities, as given in Table IV, depends much less on the choice of wave functions than the ionization probabilities themselves, we define the CSA-corrected subshell ionization probabilities in the following way:

TABLE IV. Ratio R_n of L-subshell ionization probabilities calculated with and without subshell coupling, respectively, for impact parameter $b=0$.

System	R_n		
	L_{I}	L_{II}	L_{III}
403-MeV $N^{7+}\rightarrow$La	1.01	0.95	0.96
350-MeV $N^{7+}\rightarrow$Ta	0.93	0.86	0.88
500-MeV $Ne^{10+}\rightarrow$Ta	0.88	0.79	0.82
210-MeV $N^{7+}\rightarrow$Tb	0.87	0.76	0.79
300-MeV $Ne^{10+}\rightarrow$Tb	0.82	0.64	0.68
500-MeV $Ne^{10+}\rightarrow$U	0.80	0.66	0.72

$$P_n^{\mathrm{ion}} = P_n^{\mathrm{SCA}}R_n, \quad R_n = \frac{P_n^{\mathrm{CSA}}(M_{nk})}{P_n^{\mathrm{CSA}}(M_{nk}=0)}. \qquad (3.7)$$

For the M subshells a similar CSA correction is expected, because the smaller subshell energy spacings are counterbalanced by a higher effective collision velocity (measured in terms of impact velocity with respect to Bohr velocity). However, because of the small energy shifts of the M-hole satellites, M-subshell effects are hard to see in the experimental spectra. Therefore, M-subshell coupling has not been considered in the present work.

From Table IV it is obvious that the subshell coupling leads to a reduction of the subshell ionization probabilities and hence of the total L-shell ionization probability. This effect, which is typical for coupled-channel approaches with a truncated basis like Eq. (3.5a) [33,34], is in contradiction to experimental data of impact-parameter–dependent measurements on subshell ionization [35]. It has recently been suggested [36] that a renormalization of the diagonal coupling matrix elements M_{nn}, such that M_{nn} ($R=0$)$=E_n^{ua}-E_n$ (the difference between the experimental subshell energy of the united and the separated atom) is guaranteed, will improve on the absolute value of the subshell ionization probabilities. This indicates that the molecular effects nevertheless play a non-negligible role, and that for a proper description one should enlarge the number of separated atom basis states by including continuum states of momentum comparable to the Bohr velocity of the bound states.

C. Vacancy creation due to electron capture by the projectile

When the collision velocity is of the order of or below the Bohr velocity of a particular target shell, capture of these electrons into a vacant projectile bound state gains importance. For asymmetric systems with $Z_P \ll Z_T$, capture into the projectile K shell is the dominating process, while capture into all higher bound states contributes only about 20%. Therefore, we restrict ourselves to the capture into the K shell. The capture probabilities are calculated in the strong potential Born theory (SPB) [37,38], which treats the electron-projectile interaction consistently to first order, and hence, is adequate for the present asymmetric collision systems. For electron capture from a subshell n, the probability is given by [39]

TABLE V. L-subshell capture probabilities $P^{\rm cap}$, in percent, per target electron, in nonrelativistic transverse peaked SPB, for impact parameter $b=0$.

System	L-electron capture probability, $P^{\rm cap}$ $(b=0)$ (%)		
	$L_{\rm I}$	$L_{\rm II}$	$L_{\rm III}$
403-MeV $N^{7+}\rightarrow$La	0.215	0.237	0.237
350-MeV $N^{7+}\rightarrow$Ta	0.030	0.236	0.236
500-MeV $Ne^{10+}\rightarrow$Ta	0.195	1.110	1.110
210-MeV $N^{7+}\rightarrow$Tb	0.027	0.525	0.525
300-MeV $Ne^{10+}\rightarrow$Tb	0.179	2.410	2.410
500-MeV $Ne^{10+}\rightarrow$U	0.037	0.540	0.540

$$P_n^{\rm cap}(b)=|a_{fn}|^2, \tag{3.8}$$

$$a_{fn}=-i\int_{-\infty}^{\infty}dt\int d\vec{k}\; e^{i[E_f(\vec{k})-E_n]t}e^{i\vec{k}\cdot\vec{b}}\varphi_f^{*P}(\vec{k}-\vec{v}) \times\langle\psi_{\vec{k},E_f}|V_P|\psi_n\rangle \tag{3.9}$$

with $E_f(\vec{k})=E_f^P+\vec{k}\cdot v-\vec{v}^2/2$ and $\varphi_f^P(\vec{k}-\vec{v})$ is the Fourier transform of the projectile K-shell state. For the off-shell wave function $\Psi_{\vec{k},E_f}$ the near shell limit is used,

$$\Psi_{k,E_f}\approx\left[\frac{2E_f-k^2-i\varepsilon}{4(2E_f-i\varepsilon)}\right]^{i\eta_0}\Gamma(1-i\eta_0)e^{-(\pi/2)\eta_0}\Psi_{\vec{k}},$$

$$\eta_0=\frac{Z_T}{k} \tag{3.10}$$

with $\epsilon\rightarrow 0$ and $\Psi_{\vec{k}}$ is a continuum target state. In the calculation, screened hydrogenic wave functions are used and a transverse peaking approximation is applied [39]. For our collision systems, capture from the L subshell will be the most important process since the collision velocity is close to the L-shell Bohr velocity. The L-subshell capture probabilities for impact parameter $b=0$ are listed in Table V.

Since the SPB calculation is nonrelativistic, the $L_{\rm II}(2p_{1/2})$ and $L_{\rm III}(2p_{3/2})$ wave functions have to be related to the $2p$, $m=0$ and $2p$, $|m|=1$ states by means of the spin-orbit coupling:

$$\Psi_{2p_{1/2,1/2}}=\sqrt{2/3}|2p_1\rangle\chi_{(-1/2)}-\sqrt{1/3}|2p_0\rangle\chi_{(+1/2)},$$

$$\Psi_{2p_{3/2,1/2}}=\sqrt{1/3}|2p_1\rangle\chi_{(-1/2)}+\sqrt{2/3}|2p_0\rangle\chi_{(+1/2)}, \tag{3.11}$$

$$\Psi_{2p_{3/2,3/2}}=|2p_1\rangle\chi_{(+1/2)}.$$

Exploiting the fact that at $b=0$, $P^{\rm cap}_{2p,|m|=1}=0$, one simply obtains $P^{\rm cap}_{L_{\rm II}}=\frac{1}{3}P^{\rm cap}_{2p,|m|=0}$ and $P^{\rm cap}_{L_{\rm III}}=\frac{2}{3}P^{\rm cap}_{2p,|m|=0}$ for filled subshells. Per target electron, this reduces to $P^{\rm cap}_{L_{\rm II}}=P^{\rm cap}_{L_{\rm III}}=\frac{1}{3}P^{\rm cap}_{2p,m=0}$. However, a nonrelativistic description of the target wave functions suppresses the high momentum components in its Fourier transform. Since capture proceeds via a high-lying intermediate continuum state, the contribution from these high bound-state momentum components is very important. Therefore, the heavier the target, the more a nonrelativistic theory will underestimate the capture cross sections. From comparison with experimental L-shell capture data for the impact of 24 MeV/nucleon ^{3}He on heavy targets up to gold [40], we estimate our SPB results to be a factor of 2–3 too low.

D. Multiple electron ionization cross section

The multiple electron ionization cross sections are calculated in the framework of the independent electron model. The assumption of the model is that the ionization of a particular electron is not correlated with the excitation of other electrons within the same atom.

In this case the probability $\wp_m(b)$ for ionizing m electrons from an atomic (sub)shell i consisting of n_i electrons as a function of the impact parameter b is given by the binomial distribution [41]

$$\wp_m(b)=\binom{n_i}{m}[P_i(b)]^m[1-P_i(b)]^{n_i-m}. \tag{3.12}$$

$P_i(b)$ is the subshell ionization probability per electron at the impact parameter b.

The cross section σ for the simultaneous ionization of electrons from different (sub)shells can be calculated from the product over all the (sub)shells i, which is integrated over the impact parameter b [41,42]:

$$\sigma=2\pi\int_0^{\infty}b\;db\prod_i\binom{n_i}{m_i}[P_i(b)]^{m_i}[1-P_i(b)]^{n_i-m_i}. \tag{3.13}$$

For a (sub)shell j that is not taken into account explicitly, it can easily be deduced that all its possible configurations are included as

$$\sum_{m_j=0}^{n_j}\binom{n_j}{m_j}[P_j(b)]^{m_j}[1-P_j(b)]^{n_j-m_j}=1. \tag{3.14}$$

If an average L-shell ionization probability, $P_L(b)$, is introduced, the cross section for creation of a $(1\,K,\;n\,L)$ hole atomic state, according to Eq. (3.13), is given by

$$\sigma_{1\;K,n\;L}=2\pi\int_0^{\infty}b\;db\binom{2}{1}P_K(b)[1-P_K(b)] \times\binom{8}{n}[P_L(b)]^n[1-P_L(b)]^{8-n}, \tag{3.15}$$

where $P_K(b)$ is the direct one-electron ionization probability from the K shell.

For the colliding systems under investigation, the calculated L-shell electron ionization probabilities, $P_L(b)$, change less than 20% over the entire impact parameter region (0 to $b_{\rm max}$), so we consider them as independent of the impact parameter and equal to the ionization probability at b_K. In this case the above equation can be written as

$$\sigma_{1\ K,n\ L}=\sigma(1\ K)\binom{8}{n}[P_L(\bar{b}_K)]^n[1-P_L(\bar{b}_K)]^{8-n}, \tag{3.16}$$

where $\sigma(1\,K)=2\pi\int_0^\infty b\ db\binom{2}{1}P_K(b)[1-P_K(b)]$ is the cross section for ionization of a K-shell electron.

It follows from Eq. (3.16) that the L-shell ionization probability P_L can be extracted from the relative cross-section ratio between atomic states with one K hole and different numbers of L-shell holes. From a measurement of such cross-section ratios the L-shell ionization probability can be determined experimentally (see Sec. V).

In order to account for L-subshell coupling and electron capture, the total vacancy production probability $P_i^{\rm tot}$ is given by

$$P_i^{\rm tot}=P_i^{\rm SCA}R_i+P_i^{\rm cap}, \tag{3.17}$$

where $P_i^{\rm SCA}$ is the SCA probability for direct ionization, R_i is the correction for subshell coupling defined in Eq. (3.7), and $P_i^{\rm cap}$ is the capture probability from Eq. (3.8). In our case the index i in Eq. (3.17) runs over the three L subshells (while $P_i^{\rm tot}$ is identified with $P_i^{\rm SCA}$ for other subshell states i). Since electron capture as well as subshell coupling contribute less than 30% to the L-shell vacancy production for all cases studied here, the assumptions of the independent particle model are still justified; the probability for multiple L-hole production remains small (see Fig. 2).

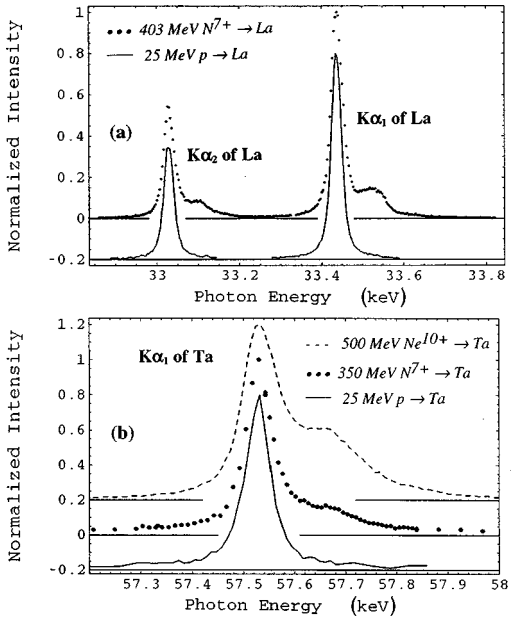

FIG. 3. (a) $K\alpha_{1,2}$ x rays of La emitted during the bombardment with 29 MeV/nucleon N^{7+} beam. The comparison with the lanthanum spectra induced during the bombardment with the 25-MeV protons reveals the satellite structure due to nitrogen bombardment. (b) Tantalum $K\alpha_1$ x rays emitted during the bombardment with 25 MeV/nucleon proton, N^{7+} and Ne^{10+} beams. The satellite structure becomes more pronounced as the projectile's nuclear charge is increased.

IV. STRUCTURE OF THE SPECTRA

During the bombardment of the target atoms with a 25 MeV proton beam, the induced $K\alpha$ spectra contain the diagram line without visible satellite structure (Fig. 3). But during heavy ion-atom collision with projectiles having about the same energy per nucleon as for the protons, the inner shells of the target atom are multiple-ionized and therefore the induced $K\alpha$ spectra reveal a satellite structure at the high-energy side of the diagram line. While the intensity of the satellite structure is increasing as the projectile's charge increases, its energy spread depends sensitively on the particular K x-ray transition and the atomic number of the target element (Fig. 3).

A. Transitions energies

The energy shifts of the $K\alpha_{1,2}$ satellite transitions in the presence of one L- or M-subshell spectator hole, relative to the $K\alpha_{1,2}$ diagram transitions, have been calculated using the Dirac-Fock code of [22]. The results obtained are listed in Table VI.

The natural widths of the $K\alpha$ x-ray diagram lines are larger than the energy differences between the diagram line and satellite transitions in the presence of an M spectator hole. In Fig. 4, the largest energy shift of a $K\alpha_1M^1$ satellite transition (originating from an $M_{\rm II}$ spectator hole) from the diagram $K\alpha_1$ transition is displayed, as a function of the target atom nuclear charge. As can be deduced, the satellite transitions in the presence of an M spectator hole are well embedded in the diagram lines.

For the rest of our discussion we define as the $K\alpha$ ''diagram'' transition, $K\alpha L^0$, a $K\alpha$ transition without the presence of the L spectator hole (indifferent for the M-, N-, or higher-shell holes), and as the $K\alpha$ ''satellite'' transition, $K\alpha L^n$, a $K\alpha$ transition in the presence of n L additional spectator hole(s).

For the medium-heavy to heavy atoms investigated here, the $K\alpha$ fine-structure energy splitting is larger than the energy shifts of the $K\alpha$ ''satellites'' (Fig. 4). So the $K\alpha_2L^1$ ''satellite'' structure may have only a minor interference with the $K\alpha_1$ spectrum and therefore can be investigated separately.

However, the study of the individual $K\alpha L^1$ x-ray ''satellites,'' originating from the presence of an L spectator hole in the various L subshells, has an inherent limitation. The energy difference between these transitions is on the order of the natural widths and this makes their distinctive study difficult (see Fig. 4 and Table VI).

Angular-momentum coupling

When a $K\alpha$ transition takes place in the presence of one L spectator hole, the initial state is made up of one hole in the K shell and one hole in the L shell and the final state of two holes in the L shell. The coupling of the angular momenta of the holes gives rise to a complex multiplet composed of many transitions. In the case of the $K\alpha_1$ transition, the three L satellite lines split into nine components and in the case of the $K\alpha_2$ transition into eight components [14,15,43].

The multiconfiguration Dirac-Fock method [22] uses j-j angular-momentum coupling, where each configuration-state wave function corresponds to a single j-j coupled state. An atomic state, however, is seldom described by a single j-j state. Usually one needs all the j-j states coupled to give the

TABLE VI. Energy shifts of the $K\alpha_{1(2)}$ satellite transitions, in the presence of an L or M subshell spectator hole, relative to the diagram $K\alpha_{1(2)}$ transition, without including the hole-hole angular-momentum coupling.

	$E(K\alpha_{1(2)}^{sat})-E(K\alpha_{1(2)}^{diag})$ (eV)							
$K\alpha_{1(2)}$ transition	Lanthanum		Terbium		Tantalum		Uranium	
Initial hole(s)→Final hole(s)	$K\alpha_1$	$K\alpha_2$	$K\alpha_1$	$K\alpha_2$	$K\alpha_1$	$K\alpha_2$	$K\alpha_1$	$K\alpha_2$
$K\rightarrow L_{III(II)}$	0.0	0.0	0.0	0.0	0.0	0.0	0.0	0.0
$KL_I\rightarrow L_{III(II)}L_I$	77.1	71.8	95.8	85.2	119.7	105.8	194.0	157.2
$KL_{II}\rightarrow L_{III(II)}L_{II}$	100.3	77.7	127.2	91.0	163.6	121.2	286.4	196.4
$KL_{III}\rightarrow L_{III(II)}L_{III}$	73.3	71.6	89.3	81.3	102.5	94.0	139.2	114.4
$KM_I\rightarrow L_{III(II)}M_I$	9.2	8.6	12.4	11.8	18.2	16.2	32.4	26.8
$KM_{II}\rightarrow L_{III(II)}M_{II}$	12.6	16.5	14.0	12.5	25.7	30.0	49.2	52.2
$KM_{III}\rightarrow L_{III(II)}M_{III}$	11.4	8.5	12.0	11.8	19.7	14.4	29.2	19.6
$KM_{IV}\rightarrow L_{III(II)}M_{IV}$	−1.3	1.8	0.4	0.2	1.4	4.7	2.9	5.3
$KM_V\rightarrow L_{III(II)}M_V$	0.4	−2.0	0.3	0.0	3.5	−0.5	4.6	−1.1

total J as obtained from the nonrelativistic configuration. Consider, for example, the $1s^{-1}2p^{-1}$ states belonging to $J=1$. This state is a superposition of two states; $a|1s2p_{1/2}\rangle + b|1s2p_{3/2}\rangle$, with relative weights a and b. The energetically lower $J=1$ state would correspond to a $K^{-1}L_{II}^{-1}$ configuration and the higher $J=1$ state would correspond to a $K^{-1}L_{III}^{-1}$ configuration. We have calculated the energies and transition rates of these multiplets for La, Tb, Ta, and U using the MCDF code (Table VII). As can be deduced from the energy values given in Table VII, the ''satellite'' transitions in the presence of L_I, L_{II}, or L_{III} spectator vacancy are not distinct but consist of transitions that are displaced and mixed.

Finally, the significance of the angular-momentum coupling between the ''active'' K and L_{III} holes with one M ''spectator'' hole during a $K\alpha_1$ transition has been investigated. For the lanthanum $K\alpha_1$ transition in the presence of an M-subshell spectator hole the five satellite transitions, with energy shifts of −1.3 to 12.6 eV (Table VI), split into 24 lines, the shifts of which extend from −8.6 to 22.4 eV [23].

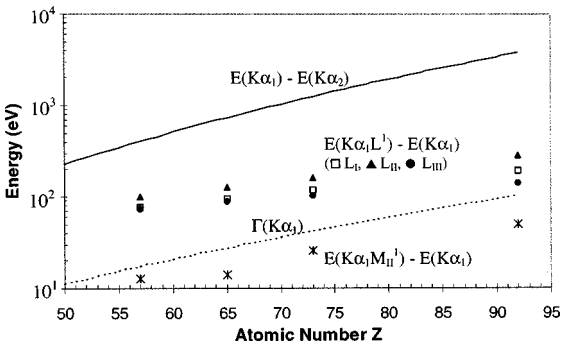

FIG. 4. Natural widths Γ of the diagram $K\alpha_1$ transition (---) and the energy fine-structure splitting between $K\alpha_1$ and $K\alpha_2$ diagram transitions (—), as a function of the atomic number Z [20,21]. Also are shown the calculated energy shift of $K\alpha_1$ satellite transitions, originating from the presence of one spectator hole in the L_I (□), L_{II} (▲), L_{III} (●), or M_{II} (∗) subshell, from the $K\alpha_1$ diagram transition for La, Tb, Ta, and U.

B. Transitions intensities

The deexcitation of the target atoms excited by the colliding ions takes place via radiative, Auger, and Coster-Kronig transitions. The observed intensity $I_j^{K\alpha_{1(2)}}$ following the deexcitation of an initial atomic state $|j\rangle$, which contains a K hole, by a $K\alpha_{1(2)}$ x-ray transition is proportional to the product

$$I_j^{K\alpha_{1(2)}} \propto \sigma_j^{obs}\omega_j^{tot}\omega_j^{K\alpha_{1(2)}}, \tag{4.1}$$

where σ_j^{obs} is the cross section of the $|j\rangle$ atomic state configuration, at the instant of the $K\alpha$ photon emission (and not at the instant of collision), and ω_j^{tot} and $\omega_j^{K\alpha_{1(2)}}$ are the total and partial fluorescence yields corresponding to the $|j\rangle$ atomic state. In the following, we discuss the evaluation method concerning cross sections, total, and partial fluorescence yields.

The observed cross section σ_j^{obs} is obtained from the initial cross sections at the time of collision, when the vacancies are created, by accounting for the rearrangement of the various atomic configuration $|i\rangle$, prior to the K x-ray emission:

$$\sigma_j^{obs} = R_{j\rightarrow j}\sigma_j^{ini} + \sum_{i\neq j} R_{i\rightarrow j}\sigma_i^{ini} + O(R^2), \tag{4.2}$$

where σ_j^{ini} and σ_i^{ini} are the initial cross sections of the $|j\rangle$ and $|i\rangle$ atomic states, respectively, $R_{j\rightarrow j}$ is the probability that the initially created $|j\rangle$ state remains unchanged, and $R_{i\rightarrow j}$ is the probability for mutation from the initial state $|i\rangle$ into the $|j\rangle$. The initial cross sections are calculated using Eq. (3.13). The last term in Eq. (4.2) describes the contribution to the observed cross section from double or higher-order rearrangement of the initial cross section prior to the observation. For the specific systems and transitions that we study here, this term is negligible.

In the case of multiply ionized states, the determination of the cross section σ_j^{obs} is a complex problem due to the large number of deexcitation and rearrangement channels and this performs the determination of the redistribution probabilities, R, a laborious duty. In order to reduce this complexity for the study of the $K\alpha$ x-ray transitions of the investigated collision

TABLE VII. Energy shifts of the satellite $K\alpha_1$ ($KL \rightarrow L_{III}L$) transition, including the angular-momentum coupling between the ''active'' K and L_{III} holes with one L ''spectator'' hole, relative to the diagram $K\alpha_1$ ($K \rightarrow L_{III}$) transition, and the corresponding $E1$ transition rates.

$K\alpha_1$ transition Initial hole(s)→Final hole(s)	$E(K\alpha_1^{sat}) - E(K\alpha_1^{diag})$ (eV)				Transition rates (10^{15} sec^{-1})			
	La	Tb	Ta	U	La	Tb	Ta	U
$K\ (J=1/2) \rightarrow L_{III}\ (J=3/2)$	0.0	0.0	0.0	0.0	10.23	17.30	31.3	83.2
$KL_I\ (J=0) \rightarrow L_{III}L_I\ (J=1)$	108.1	137.0	176.0	307.0	8.69	15.69	29.7	82.0
$KL_I\ (J=1) \rightarrow L_{III}L_I\ (J=1)$	21.0	26.0	36.0	64.0	2.30	3.54	6.0	14.8
$KL_I\ (J=1) \rightarrow L_{III}L_I\ (J=2)$	78.1	96.0	118.0	181.0	8.64	14.60	26.4	70.0
$KL_{II}\ (J=0) \rightarrow L_{III}L_{II}\ (J=1)$	116.2	152.0	200.0	375.0	11.04	17.58	31.8	84.5
$KL_{II}\ (J=1) \rightarrow L_{III}L_{II}\ (J=1)$	109.3	134.0	168.0	254.0	1.65	2.78	5.1	13.8
$KL_{II}\ (J=1) \rightarrow L_{III}L_{II}\ (J=2)$	92.4	116.0	149.0	237.0	9.56	15.29	27.2	71.2
$KL_{III}\ (J=1) \rightarrow L_{III}L_{III}\ (J=0)$	58.8	68.0	80.0	108.0	3.43	5.82	10.5	27.9
$KL_{III}\ (J=1) \rightarrow L_{III}L_{III}\ (J=2)$	101.0	119.0	140.0	192.0	8.19	15.03	25.8	69.4
$KL_{III}\ (J=2) \rightarrow L_{III}L_{III}\ (J=2)$	69.1	80.0	96.0	132.0	5.39	8.47	16.1	42.4

systems, we only consider the holes' movement in the K and L subshells but ignore possible rearrangements in the $M,N,\ldots$ shells. This is a reasonable approximation, as has been illustrated in the preceding section, due to the fact that the satellite transitions in the presence of an $M,N,\ldots$ spectator hole(s) are well embedded in their ''diagram'' line.

The consequences of this approach are as follows.

(i) An initial $|1K,\ 0L\rangle$ hole configuration remains unchanged until the K x-ray transition, detached from what happens in the higher shells. Consequently, in this case the redistribution probability $R_{(1K,0L \rightarrow 1K,0L)}$ is equal to unity.

(ii) In the case of an initial $|1K,\ 1L_x\rangle$ hole configuration, the L_x hole may decay to an M or higher shell through a radiative process, with a probability given by the fluorescence yield ω_{L_x}, or through an Auger process, with a probability given by the Auger yield a_{L_x} (Fig. 5). If the L-hole decay takes place prior to the K x-ray transition (during the lifetime of the K hole), the newly created atomic state corresponds to a $|1K,\ 0L\rangle$ configuration.

(iii) In the case of an initial $|1K,\ 1L_x\rangle$ hole configuration, the L_x may decay through a Coster-Kronig process, with a probability given by the Coster-Kronig yield f_{L_x} ($\omega_{L_x} + a_{L_x} + f_{L_x} = 1$) (Fig. 5). If the L_x-hole decay takes place prior to the K x-ray transition, the L hole will be found in a different L subshell than the initial, but the state remains as $|1K,\ 1L\rangle$ configuration.

Based on the discussion above and according to Eq. (4.2), the cross sections σ_j^{obs} for the atomic configurations $|1K,\ 0L\rangle$, $|1K,\ 1L_I\rangle$, $|1K,\ 1L_{II}\rangle$, and $|1K,\ 1L_{III}\rangle$, assuming that there are no contributions from $|1K,\ 2L\rangle$ hole states, are given by

$$\begin{pmatrix} \sigma^{obs}_{1K,0L} \\ \sigma^{obs}_{1K,1L_I} \\ \sigma^{obs}_{1K,1L_{II}} \\ \sigma^{obs}_{1K,1L_{III}} \end{pmatrix} = \begin{pmatrix} 1 & \frac{\Gamma_{L_I}}{\Gamma_{L_I}+\Gamma_K}(\omega_{L_I}+a_{L_I}) & \frac{\Gamma_{L_{II}}}{\Gamma_{L_{II}}+\Gamma_K}(\omega_{L_{II}}+a_{L_{II}}) & \frac{\Gamma_{L_{III}}}{\Gamma_{L_{III}}+\Gamma_K} \\ 0 & \frac{\Gamma_K}{\Gamma_{L_I}+\Gamma_K} & 0 & 0 \\ 0 & \frac{\Gamma_{L_I}}{\Gamma_{L_I}+\Gamma_K} f_{L_I \rightarrow L_{II}} & \frac{\Gamma_K}{\Gamma_{L_{II}}+\Gamma_K} & 0 \\ 0 & \frac{\Gamma_{L_I}}{\Gamma_{L_I}+\Gamma_K} f_{L_I \rightarrow L_{III}} & \frac{\Gamma_{L_{II}}}{\Gamma_{L_{II}}+\Gamma_K} f_{L_{II} \rightarrow L_{III}} & \frac{\Gamma_K}{\Gamma_{L_{III}}+\Gamma_K} \end{pmatrix} \begin{pmatrix} \sigma^{ini}_{1K,0L} \\ \sigma^{ini}_{1K,1L_I} \\ \sigma^{ini}_{1K,1L_{II}} \\ \sigma^{ini}_{1K,1L_{III}} \end{pmatrix}, \tag{4.3}$$

where Γ denotes the level widths of K and L subshells, and ω, a, and f are the L-subshell fluorescence, Auger and Coster-Kronig yields, respectively. The matrix elements that represent the redistribution probabilities during the lifetime of the K hole are calculated using the values for the K and L level widths and the L deexcitation yields for singly ionized atoms as given by [20]. The redistribution probabilities $R_{(1K,1L_x \rightarrow 1K,0L)}$ for mutation from the atomic configuration $|1K,\ 1L_x\rangle$ to the $|1K,\ 0L\rangle$ are given in Table VIII. An inspection of this table shows that the x-ray spectra of heavy elements are less affected by relaxation processes than the light elements, and thus the observed spectra reflect more the initial states created during the collision. This underlines one of the advantages of using heavy Z elements as targets.

Dealing with the L shell as a mean over the different L subshells, the observed cross section $\sigma^{obs}_{1K,0L}$ for the atomic

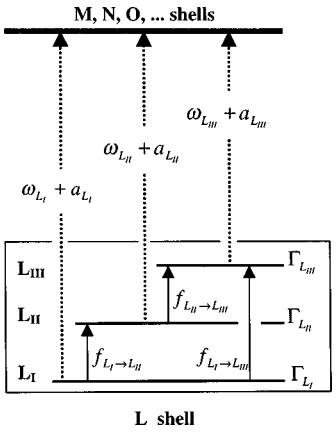

FIG. 5. Radiative, Auger, and Coster-Kronig deexcitation channels from the L subshells of the target atoms. Their relative rates are given by the fluorescence ω_{L_x}, Auger a_{L_x}, and Coster-Kronig f_{L_x} yields, respectively. The level widths of the L subshells are given by Γ_{L_x}, while the effective mean width $\Gamma_L^{\rm eff}$ of the L shell is given by Eq. (4.5).

configuration $|1K,\ 0L\rangle$ is given, according to Eq. (4.2), by

$$\sigma^{\rm obs}_{1K,0L}=1\times\sigma^{\rm ini}_{1K,0L}+\frac{\Gamma_L^{\rm eff}}{\Gamma_L^{\rm eff}+\Gamma_K}\,\sigma^{\rm ini}_{1K,1L}, \tag{4.4}$$

where Γ_K is the K level width and $\Gamma_L^{\rm eff}$ is the effective width of the L shell, which is defined as

$$\Gamma_L^{\rm eff}=C_{L_{\rm I}}\Gamma_{L_{\rm I}}(\omega_{L_{\rm I}}+\alpha_{L_{\rm I}})+C_{L_{\rm II}}\Gamma_{L_{\rm II}}(\omega_{L_{\rm II}}+\alpha_{L_{\rm II}})+C_{L_{\rm III}}\Gamma_{L_{\rm III}} \tag{4.5}$$

with

$$C_{L_{\rm I}}+C_{L_{\rm II}}+C_{L_{\rm III}}=1, \tag{4.6}$$

where C_{L_x} are weighting coefficients describing the contribution of the individual L subshell to the mean L state. For a statistical contribution of the L subshells we have $C_{L_{\rm I}}=0.25$, $C_{L_{\rm II}}=0.25$, and $C_{L_{\rm III}}=0.50$. Using the prediction of the SCA-OPM (Table II), we get for all our systems values close to $C_{L_{\rm I}}=0.14$, $C_{L_{\rm II}}=0.29$, and $C_{L_{\rm III}}=0.57$. The estimates for the effective width, $\Gamma_L^{\rm eff}$, for the different sets of weighting coefficients are shown in Table IX. We emphasize that in general for the precise estimation of the effective width the knowledge of the weighting coefficients C_{L_x} is mandatory.

The relative uncertainty in the determination of the effective width $\Gamma_L^{\rm eff}$ for the two different distributions is at maximum 4%, while the errors in the knowledge of L-subshell level widths is on the order of 15% and the K level widths it is around 5% [20]. In the case of multiple ionized systems, a more severe problem is the lack of data on the level widths in the presence of the spectator holes. It has been estimated that in the case of lanthanum the K level width can vary as much as 15% in the presence of an L spectator hole [44]. An overall error in the order of 20% is estimated for the determination of the redistribution factors R.

The total K fluorescence yield $\omega^{\rm tot}_{(1K,0L)}$ for a singly K ionized lanthanum, terbium, tantalum, and uranium atom is 0.928, 0.969, 0.983, and 0.969, respectively [45]. To our knowledge there are no data for total K fluorescence yields for high-Z elements in the presence of spectator holes. We performed a detailed theoretical calculation using the MCDF code [22] and found that $\omega^{\rm tot}_{(1K,1L_x)}$ does not change by more than 3% in the presence of a specific L_x subshell spectator hole [44]. The mean fluorescence yield $\omega^{\rm tot}_{(1K,1L)}$ of a K transition in the presence of one L spectator hole, distributed at the various L subshells, either ''statistically'' ($C_{L_{\rm I}}$:$C_{L_{\rm II}}$:$C_{L_{\rm III}}$=2:2:4) or according to the ''SCA-OPM'' predictions ($C_{L_{\rm I}}$:$C_{L_{\rm II}}$:$C_{L_{\rm III}}$=1:2:4), is within less than 1% equal to the total K fluorescence yield, $\omega^{\rm tot}_{(1K,0L)}$, of the ''diagram'' line.

Finally we have calculated *the partial K fluorescence yields* in the presence of a spectator hole for the different L subshells using first the MCDF code [22] and second a semiempirical formula that reproduces the partial yields with very good accuracy compared to the *ab initio* calculations [44]. As can be seen in Fig. 6, for the atom of lanthanum the partial yields $\omega^{K\alpha_{1(2)}}_{(1K,1L_x)}$ change considerably in the presence of a specific L spectator hole. Nevertheless, the mean fluorescence yield $\omega^{K\alpha_{1(2)}}_{(1K,1L)}$ for a $K\alpha_{1,2}$ transition, with one L spectator hole distributed either ''statistically'' or according to ''SCA-OPM'' predictions over all L subshells, is almost identical with the $K\alpha_{1,2}$ fluorescence yield of the diagram line (no L hole).

V. RESULTS

A. Comparison of the experimental *L*-shell ionization probabilities with theory

The experimental L-shell ionization probability $P_L^{\rm expt}$ can be extracted from the measured spectra in the following way:

TABLE VIII. Redistribution probabilities R for mutation from the atomic configuration $|1K,\ 1L_x\rangle$ to the $|1K,\ 0L\rangle$ during the lifetime of the K hole, according to the matrix elements in Eq. (4.3) for the various target elements.

Target element	Redistribution probabilities R		
	$\lvert1K,\ 1L_{\rm I}\rangle\to\lvert1K,\ 0L\rangle$	$\lvert1K,\ 1L_{\rm II}\rangle\to\lvert1K,\ 0L\rangle$	$\lvert1K,\ 1L_{\rm III}\rangle\to\lvert1K,\ 0L\rangle$
Lanthanum	0.117	0.175	0.195
Terbium	0.091	0.134	0.148
Tantalum	0.070	0.107	0.115
Uranium	0.044	0.072	0.072

TABLE IX. Calculated effective width Γ_L^{eff} of the L level for the target elements according to Eq. (4.5). We assume two different distributions for L subshell hole creation: the ''statistical,'' based on the statistical probability for creation of a specific L-subshell hole for which $C_{L_{\text{I}}}:C_{L_{\text{II}}}:C_{L_{\text{III}}}=2:2:4$, and the ''SCA,'' based on the theoretical predictions of the SCA-OPM for which $C_{L_{\text{I}}}:C_{L_{\text{II}}}:C_{L_{\text{III}}}=1:2:4$.

Target element	L level width, Γ_L^{eff} (eV)	
	''Statistical''	''SCA''
Lanthanum	3.01	3.13
Terbium	3.67	3.84
Tantalum	4.34	4.55
Uranium	6.81	7.06

Starting from Eqs. (4.1) and (3.16) and based on the previous discussion, the ratio between the intensity, $I_{1K,0L}^{K\alpha_{1(2)}}$, of the ''diagram'' line, $(K\alpha_{1(2)}L^0)$, to the entire intensity, $I_{1K}^{K\alpha_{1(2)}}$, of the $K\alpha_{1(2)}$ complex spectrum can be expressed as a function of the mean L-shell ionization probabilities according to

$$\frac{I_{1K,0L}^{K\alpha_{1(2)}}}{I_{1K}^{K\alpha_{1(2)}}}=\frac{\sigma_{1K,0L}^{\text{obs}}\omega_{1K,0L}^{\text{tot}}\omega_{1K,0L}^{K\alpha_{1(2)}}}{\sigma_{1K}^{\text{obs}}\omega_{1K}^{\text{tot}}\omega_{1K}^{K\alpha_{1(2)}}}$$
$$\approx(1-P_L^{\text{expt}})^8\left[1+R_{1K,1L\rightarrow 1K,0L}\frac{8P_L^{\text{expt}}}{1-P_L^{\text{expt}}}\right], \tag{5.1}$$

where the first term on the right side reflects the directly created $(1K,0L)$ hole atomic state, while the second term corresponds to the $(1K,0L)$ hole atomic originating from the initially created $(1K,1L)$ hole atomic state, in which the L-shell vacancy is being filled prior to the K x-ray emission, with a probability given by the redistribution factor $R_{1K,1L\rightarrow 1K,0L}$. As mentioned earlier, the contribution to the $(1K,0L)$ hole configurations developed in two or more step processes is of minor importance for the studied systems and hence is neglected. The total and partial fluorescence yields for the various hole atomic states are considered equal, according to the discussion of Sec. IV B.

In order to calculate the relative intensity of the ''diagram'' line, $I_{1K,0L}^{K\alpha_{1(2)}}$, with respect to the total intensity, $I_{1K}^{K\alpha_{1(2)}}$, the experimental spectra have been approximated by a superposition of Voigt profiles. To extract the results, we use the ''averaging'' fit model dealing with the L shell as a mean of the different L subshells.

We use a Voigt function to describe the ''diagram'' line, $K\alpha_{1(2)}L^0$, with Lorentz and Gauss widths being free parameters. According to the energy considerations of the preceding section, in the case of the ''diagram'' line, transitions in the presence of the M spectator hole fall within its natural linewidth. So, despite its composite structure, a single Voigt function is sufficient to describe the shape of the ''diagram'' line, having a Lorentzian width of the order of the natural width of a singly ionized atom and a Gaussian width that mainly describes the experimental response function and the presence of the $M,N,\ldots$ spectator holes [46,47]. In order to describe the $K\alpha_{1(2)}L^1$ structure, a second Voigt function with equal Lorentzian width but free Gaussian width has been used. Finally, a third Voigt function has been used to describe spectra with $K\alpha_{1(2)}L^2$ structure.

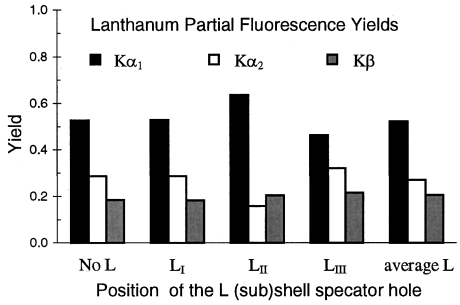

FIG. 6. Calculated partial K fluorescence yields of lanthanum with or without the presence of one spectator hole in the corresponding L subshells.

In the framework of the ''averaging'' fitting model, the energy differences of the ''satellite'' transitions from the ''diagram'' line are fixed according to the MCDF code predictions. The energy difference $E(K\alpha_{1(2)}L^1-K\alpha_{1(2)}L^0)$ has been calculated from the individual $E(K\alpha_{1(2)}L_x^1-K\alpha_{1(2)}L^0)$ differences $(x\rightarrow\text{I,II,III})$ (Table VI) using the weighting coefficients C_{L_x} [see discussion following Eq. (4.6)]. The resulting energy differences, using either ''statistical'' or ''SCA'' distributions for the L-subshell spectator hole creation, are given in Table X. For both distributions the energy differences are almost identical.

Fixed energy differences have to be used in the fit procedure in order to avoid systematic errors. Only for ''satellite'' structures well enhanced or well resolved from the ''diagram'' line was a free fitted energy difference found to be in agreement with the calculated energy differences. As an example, for the 300-MeV $Ne^{10+}\rightarrow$Tb the fit yields for the energy difference $E(K\alpha_1L^1-K\alpha_1L^0)$ 100.8 eV, in agreement with the theoretical prediction of 101.1 eV. But this is not possible for uranium, where the satellite structure cannot be resolved from the diagram line.

The high-resolution $K\alpha_{1,2}$ x-ray spectra and their fit according to the ''averaging'' model are shown in Fig. 7. The extracted Lorentzian widths of the diagram lines are listed in Table X. Their comparison with the natural width of the corresponding K x-ray transitions of single ionized atoms are in general in good agreement. The measured Lorentzian widths are somewhat larger than the natural widths due to the presence of $M,N,\ldots$ satellite transitions, which are embedded in the ''diagram'' line.

The mean L ionization probabilities, P_L^{expt}, as extracted according to Eq. (5.1), from the relative intensity of the ''diagram line'' $K\alpha_{1(2)}L^0$ to the total intensity of the $K\alpha_{1(2)}$ spectrum, are given in Table XI. The uncertainty in the determination of the ionization probabilities is due to the approximations in the derivation of Eq. (5.1), the uncertainties in the determination of the intensity ratio, and the uncertainty in the redistribution factor $R_{1K,1L\rightarrow 1K,0L}$.

The uncertainty in the intensity determination mainly originates from the ''averaging'' model, as the statistical error is at least one order of magnitude smaller. To estimate the systematic errors originating from the ''averaging''

TABLE X. Extracted Lorentzian width of the ''diagram,'' $K\alpha_{1(2)}L^0$ lines compared with the natural linewidth of the $K\alpha_{1,2}$ diagram transitions of the target atoms [20]. Also are given the calculated energy differences between the $K\alpha_{1(2)}L^1$ and $K\alpha_{1(2)}L^0$ structures assuming the ''statistical'' and the ''SCA'' distributions for L-subshell hole creation, respectively.

	$K\alpha_1L^0$ width (eV)		$E(K\alpha_1L^1-K\alpha_1L^0)$ (eV)	
System	This work	Krause [20]	''Statistical''	''SCA''
403-MeV $N^{7+}\rightarrow$La	20.0	17.6	81.0	81.6
350-MeV $N^{7+}\rightarrow$Ta	50.0	42.6	122.1	122.4
500-MeV $Ne^{10+}\rightarrow$Ta	49.9	42.6	122.1	122.4
210-MeV $N^{7+}\rightarrow$Tb	28.0	27.9	100.4	101.1
300-MeV $Ne^{10+}\rightarrow$Tb	27.5	27.9	100.4	101.1
500-MeV $Ne^{10+}\rightarrow$U	101.3	103.5	189.7	189.1
	$K\alpha_2L^0$ width (eV)		$E(K\alpha_2L^1-K\alpha_2L^0)$ (eV)	
System	This work	Krause [20]	''Statistical''	''SCA''
403-MeV $N^{7+}\rightarrow$La	20.5	17.8	73.2	73.4
210-MeV $N^{7+}\rightarrow$Tb	31.1	28.2	84.7	84.6

model, we repeated the fit of the spectra adjusting various fit parameters. As mentioned in Sec. IV B, the total uncertainty in the intensity redistribution factor, R, is about 20%, which leads to a relative uncertainty in the ionization probabilities on the order of 5%. Therefore, we estimate a total uncertainty of the ionization probabilities on the order of 10–20 %.

The theoretical mean L-shell ionization probabilities, for impact parameter $b=b_K$, as calculated with the SCA theory using either relativistic wave functions (SCA-OPM) or relativistic screened hydrogenic wave functions (SCA-HYD), are listed in Table XI. In Fig. 8 we present the ratio of the experimental data to the theoretical direct ionization predictions as a function of the reduced velocity η (in the cases for which both $K\alpha_1$ and $K\alpha_2$ spectra have been measured, we use the averaged values).

We find good agreement between the experimental and the SCA-OPM values. The deviations are on the order of 10%, except for the system 500-MeV $Ne^{10+}\rightarrow$Ta and 500-MeV $N^{7+}\rightarrow$Tb, where they are on the order of 20%. In contrast, the results of the SCA-HYD calculations deviate from the experimental values by 50–90%. The only exception is the system 500-MeV $Ne^{10+}\rightarrow$U, where the two calculations give comparable results. For all the other systems we find that generally the SCA-OPM model yields a much better description of the L-shell ionization probability than the SCA-HYD model. For the 403-MeV $N^{7+}\rightarrow$La system ($\eta_L=1.24$) this conclusion has been stated earlier [15] and has been confirmed for light, less energetic, systems [10].

We also calculated the contributions to the vacancy production probabilities for electron capture (Table V) and subshell coupling (Table IV). The inclusion of electron capture increases the vacancy production probabilities at most by 20% with respect to the direct ionization probabilities. On the other hand, the subshell coupling leads to a reduction of the ionization probabilities. However, as noted earlier, this reduction is likely to be overestimated due to the truncation of the basis states included in the coupled-channel code. The total ionization probability P^{tot}, calculated according to Eq. (3.17), is listed in Table XI.

Figure 9 shows the comparison of the L-shell ionization probabilities extracted from experiment with the theoretical values. In general, we find that these two processes, due to mutual cancellations, change the ionization probabilities by about 5–10% (except for uranium), which is in the order of the experimental uncertainty. Hence, although capture as well as subshell coupling may be important in its own, the combined effect gives little influence on the L-shell vacancy production probabilities except possibly for the heaviest collision system.

B. Construction of the theoretical spectrum and comparison with experiment

For a further comparison between experiment and theoretical predictions and as an independent analysis, we have constructed the theoretical spectra from the calculated relative intensities and energy shifts and compared them directly with the experimental spectra (for details, see [15]). The way of calculations are described in Secs. III and IV. We emphasize that this way of analysis treats the L subshells individually and not as an ''average.''

The calculated intensities are converted into the spectral parameters (linewidth and peak intensity). The line shapes of the satellite transitions, with their energy positions fixed relative to the diagram transition line, are superimposed and the resulting complex is compared to the experimental spectrum by normalizing the peak position and the peak intensity of the diagram line.

We further investigated the significance of the hole-hole angular-momentum coupling between an L spectator hole and the active K and $L_{\mathrm{III(II)}}$ holes during the $K\alpha_{1(2)}$ transition. Here, the lanthanum $K\alpha_2$ spectrum is best suited to confirm the role of the jj coupling between the inner holes. Ignoring the hole-hole angular-momentum coupling, the three $K\alpha_2L^1$ ''satellite'' transitions have almost the same energy shift from the ''diagram'' line: 71.8, 77.7, and 71.6 eV for one spectator hole in the L_{I}, L_{II}, and L_{III} subshell, respectively (Table VI), and they are larger than the natural width and the energy resolution. Therefore, the correspond-

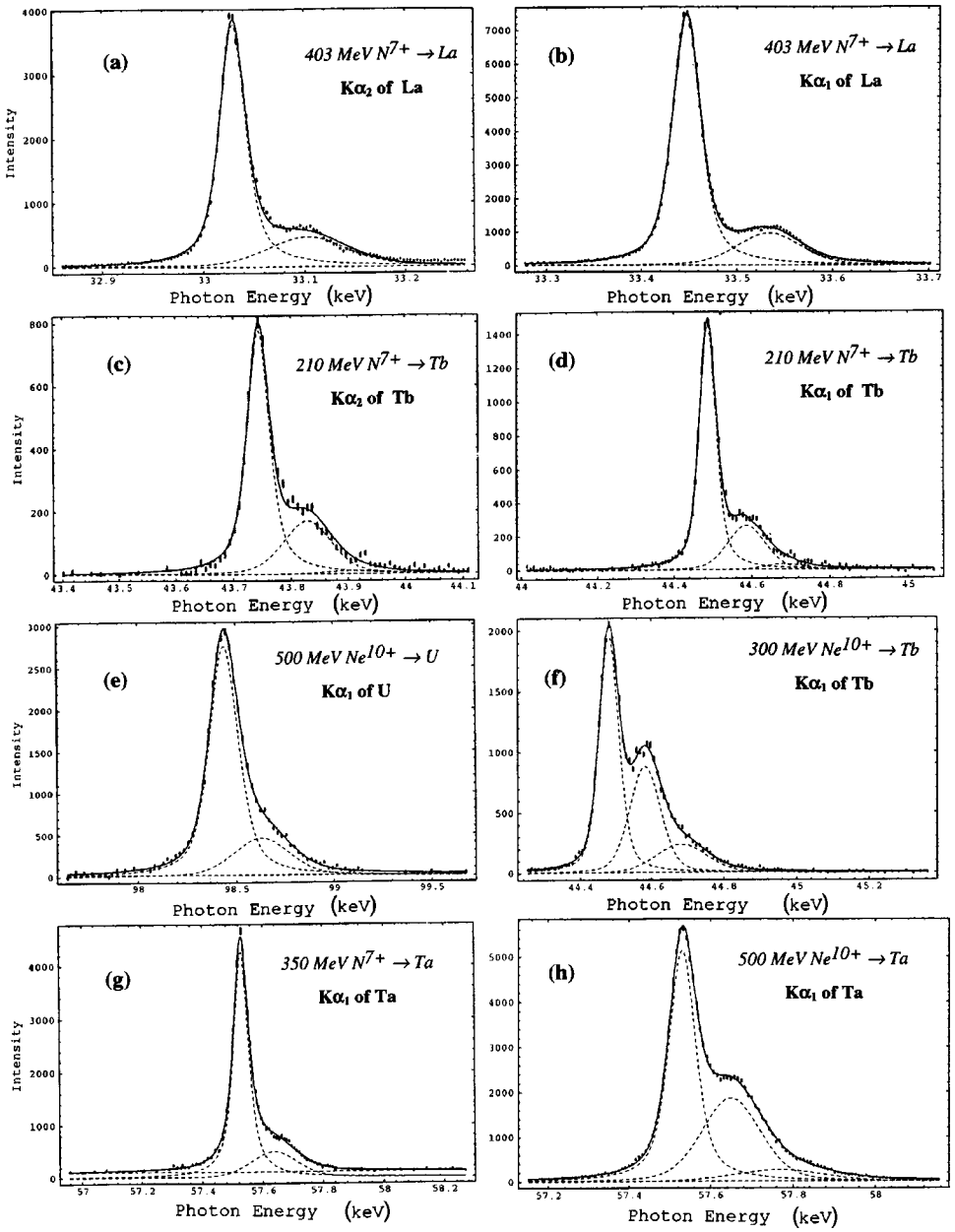

FIG. 7. $K\alpha_{1,2}$ spectra of La, Tb, Ta, and U induced by heavy ion bombardment. Results of the fitting procedure based on the ''averaging'' model (see text) are also shown.

ing satellite lines should be separated from the diagram line and show up as a pronounced bump in this energy region. But in reality the experimental spectrum exhibits a plateau-like shoulder (Fig. 7).

To confirm, we constructed the theoretical $K\alpha_2$ spectrum ignoring the hole-hole angular-momentum coupling. The K and L direct ionization probabilities are used as predicted from the SCA-OPM theory, including the subshell coupling and the electron capture (only for this particular theoretical spectrum did we include distinctly the transitions due to the presence of the M spectator hole; the M direct ionization probabilities calculated using the SCA-OPM theory are given in Table II and the energies from Table VI). A total of 150 satellite lines have been superimposed to construct the theoretical spectrum. In Fig. 10(a) the experimentally observed $K\alpha_2$ complex is compared with the theoretical predictions. The normalization between theory and experiment was extended over the energy region from the low-energy side up to 25 eV on the high-energy side of the diagram line. This region allows a satisfactory determination of peak position and height and we also avoid the interference with the $K\alpha_2 L^1$ satellite structure. The discrepancy between the experimental spectrum and the theoretical spectrum is obvious, noting the normalized χ^2 of 13.8.

Now we redo the analysis including the hole-hole angular-momentum coupling between the L spectator hole and the initial K and final L_{II} holes. This is an extensive procedure in which we handled up to 250 transitions for the description of the $K\alpha_2$ complex. The comparison between theory and experiment is drastically improved ($\chi^2 = 4.4$) [Fig. 10(b)]. The small deviation beyond 33.20 keV is to be attributed to the low energy of the $K\alpha_1$. Due to energy resolution reasons, the effect of the hole-hole coupling is especially visible for middle-heavy Z elements (Fig. 4).

TABLE XI. Experimental mean L-shell ionization probabilities P_L^{expt}, in percent, per target electron. Also is given the theoretical mean L-shell direct ionization probabilities $\overline{P}_L^{\text{SCA}}$ in percent, based on optimized-potential (OPM) wave functions and screened hydrogenic (HYD) wave functions, for impact parameter $\overline{b}_K$. The last column gives the theoretical mean L-shell ionization probabilities, P_L^{tot}, based on the SCA-OPM theory, including the contributions of the subshell coupling and of the electron capture of the L target electron from the projectile [the latter two processes taken at $b=0$, see Eq. (3.17)].

		Experiment	Theory		
			$\overline{P}_L^{\text{SCA}}(\overline{b}_K)$ (%)		
System	Observed transition	P_L^{expt} (%)	SCA-OPM	SCA-HYD	$\overline{P}_L^{\text{tot}}(\overline{b}_K)$ (%)
403-MeV $N^{7+}\rightarrow$La	$K\alpha_1$	3.7 ± 0.2	3.58	2.31	3.68
	$K\alpha_2$	4.0 ± 0.2			
350-MeV $N^{7+}\rightarrow$Ta	$K\alpha_1$	3.1 ± 0.2	2.96	1.95	2.79
500-MeV $Ne^{10+}\rightarrow$Ta	$K\alpha_1$	7.7 ± 0.4	6.10	4.03	5.86
210-MeV $N^{7+}\rightarrow$Tb	$K\alpha_1$	4.8 ± 0.3	4.00	2.79	3.56
	$K\alpha_2$	5.1 ± 0.4			
300-MeV $Ne^{10+}\rightarrow$Tb	$K\alpha_1$	9.0 ± 0.5	8.29	5.82	7.49
500-MeV $Ne^{10+}\rightarrow$U	$K\alpha_1$	3.5 ± 0.4	3.79	3.00	3.11

For a comparison of the theoretical predictions of SCA-OPM and SCA-HYD, the $K\alpha_1$ x-ray spectra during the 403-MeV $N^{7+}\rightarrow$La, 350-MeV $N^{7+}\rightarrow$Ta, and 500-MeV $Ne^{10+}\rightarrow$U collisions are studied. We selected these three systems because they cover the range of examined reduced velocity η, and of the target atomic number (from $Z=57$ to 92). In addition, in these cases contributions from the presence of two L spectator holes are negligible (less than 3%), facilitating the construction of the theoretical spectra. Subshell coupling and electron capture have not been included here.

The 403-MeV $N^{7+}\rightarrow$La system has the largest projectile velocity of all our systems, exceeding the orbiting velocity v_L of the L-shell electrons by about 25%. In Figs. 11(a) and 11(b), the experimentally observed $K\alpha_1$ complex is compared with the theoretical predictions. Comparison of experiment with the two model calculations clearly shows the superior quality of the OPM model. It is obvious from the $\chi^2=1.9$ in the case of the SCA-OPM compared to $\chi^2=19.6$ in the hydrogenic case. The results for the 350-MeV $N^{7+}\rightarrow$Ta system are shown in Figs. 11(c) and 11(d). As in the previous case, the OPM functions yield better agreement with the experiment ($\chi^2=2.10$) than hydrogenic wave functions ($\chi^2=6.58$). The results for 500-MeV $Ne^{10+}\rightarrow$U are displayed in Figs. 11(e) and 11(f). Here the projectile velocity is 60% of the L target-electron velocity. Both theoretical models are in reasonable agreement with the measured spectrum. It is also confirmed by the results using the ''averaging'' model.

For all studied systems the results obtained from the detailed analysis are consistent with our results from the ''averaging'' model (see Fig. 8 and Table XI). This also confirms the accuracy of the experimental L-shell vacancy probabilities.

VI. CONCLUSION

We have measured the $K\alpha_{1,2}$ x-ray satellite spectra of high-Z elements produced in energetic collisions by N and Ne projectiles with a high-resolution crystal spectrometer. The projectile velocity, which varied from 60% to 125% of the target L electron velocity, allowed a comparison of the experimental data with the theoretical predictions as a function of the reduced velocity.

Two independent methods of analysis of the experimental spectra were applied in order to deduce the maximum feasible information, to elucidate the complex structure, and to

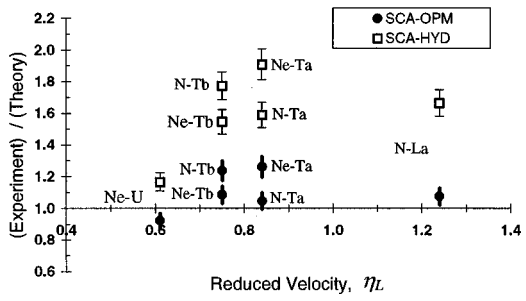

FIG. 8. Ratio of the experimental L-shell ionization probabilities for the target electrons to the SCA theoretical L-shell electron direct ionization probabilities, plotted as a function of the reduced velocity η_L.

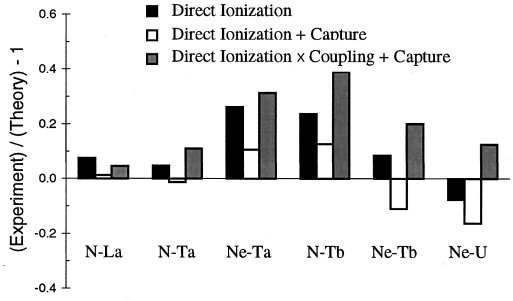

FIG. 9. Deviation from unity of the ratio between the experimental L-shell ionization probability of the target electrons to the theoretical SCA-OPM L-shell electron direct ionization probabilities, corrected for capture of the L-shell target electron by the incoming projectile and for the influence of the subshell coupling, for the various colliding systems.

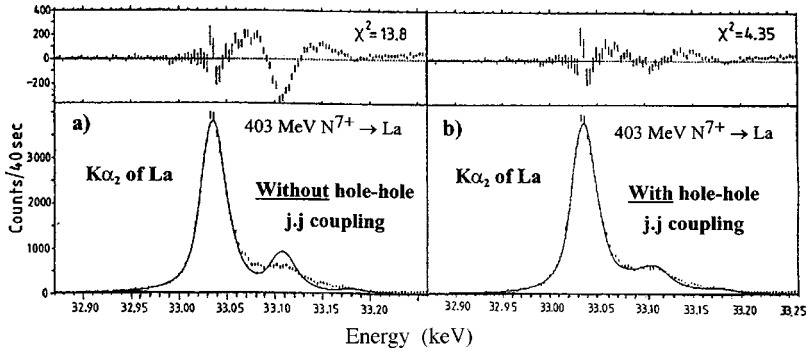

FIG. 10. Comparison of the measured (points) $K\alpha_2$ lanthanum spectrum induced by 403-MeV N^{7+} with the theoretical one (full line). The theoretical spectrum has been constructed using the SCA-OPM direct ionization probabilities modified by the subshell coupling and including the electron capture. The deviations between theory and experiment are shown in the upper part of the figures. (a) The hole-hole angular-momentum coupling between the initial-state K hole and the final-state L_{II} hole with one L ''spectator'' hole is not included (Table VI). (b) The angular-momentum coupling between the ''active'' and ''spectator'' holes is included (Table VII).

exclude systematic errors. In the first, so-called ''empirical'' one, we deal with the L shell as a mean over the different L subshells and in the second, so-called ''*ab initio*'' one, the contributions of the various L subshells were taken into account explicitly. Common principles in the two approaches are the inclusion of the relaxation processes, which change the electron configuration between the creation of the vacancies and their decay as well as variations of $K\alpha$ fluorescence yields in the presence of L spectator holes. Also the multiionized states were handled in the framework of the indepen-

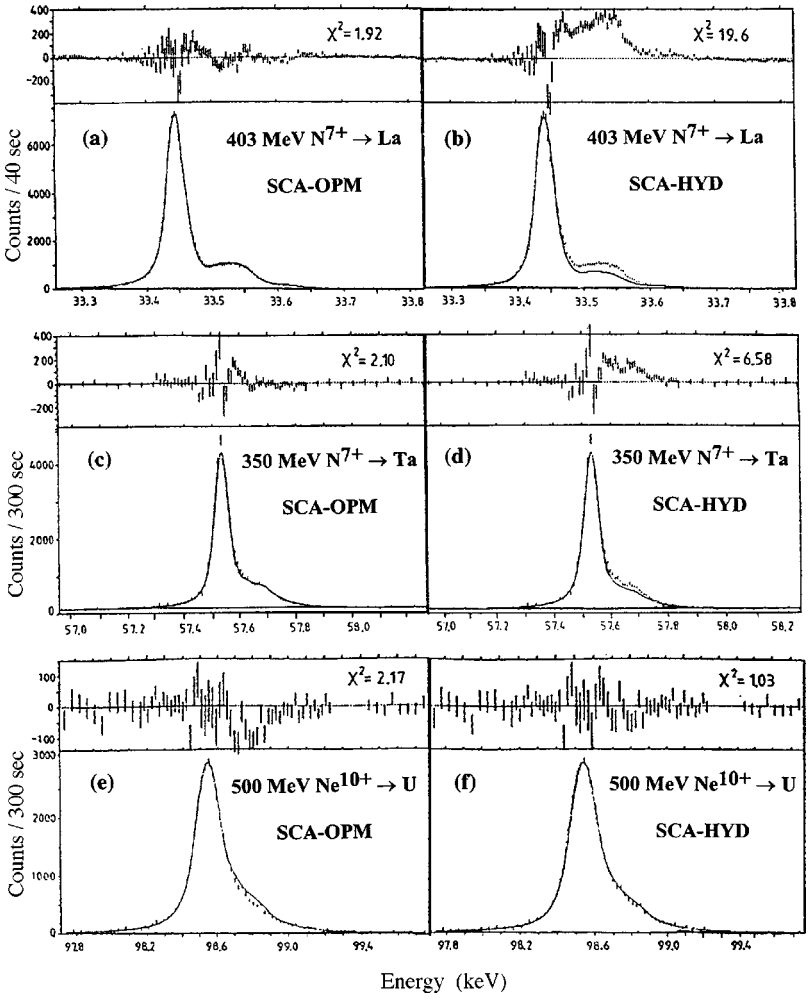

FIG. 11. Comparison of the measured (points) $K\alpha_1$ x-ray spectra during the 403 $N^{7+}\rightarrow$La, 350 $N^{7+}\rightarrow$Ta, and 500 $Ne^{10+}\rightarrow$U collisions with the theoretical line shape (full line). For the construction of the theoretical spectra the intensities have been calculated using the direct ionization probabilities according to SCA-OPM [(a), (c), and (e)] and SCA-HYD [(b), (d), and (f)] predictions. The effects of subshell coupling and electron capture have not been included.

dent electron model (using the binomial distribution).

In the empirical analysis the $K\alpha$ complex was fitted with up to three Voigt lines. The mean L-shell ionization probabilities for impact parameters within the K shell of the target atom were extracted. But this way of analysis cannot describe the details of the line shape.

In the *ab initio* analysis the experimental spectra were compared with detailed theoretical spectra, treating individually the various L subshells. This method of analysis is complementary to the empirical one, as it does not allow a direct extraction of the ionization probabilities but warrants an accurate description of the complex line shapes. Its sensitivity on the line shape allowed us to demonstrate for middle-heavy Z elements the importance of the hole-hole angular momentum coupling between the ''active'' K and L holes and one L ''spectator'' hole during the $K\alpha_{1,2}$ transitions.

The results from both methods of analysis are consistent. They were compared with the theoretical predictions of the direct ionization probabilities for a single electron, calculated in the first-order perturbation approximation (SCA) using either Dirac-Fock-type wave functions (SCA-OPM) or relativistic hydrogenlike ones (SCA-HYD). The predictions based on the SCA-OPM calculations are in good agreement with the experimental results for the range of reduced velocities considered, in contrast to the SCA-HYD calculations. The relativistic hydrogenic wave functions only provide a reliable description of experimental data if ionization of a deep-lying inner shell is considered and if the collision velocity is low enough such that the main contribution to the ionization cross section comes from distances of the order of the radii of these shells. This criterion was fulfilled only for the case of L-shell ionization in 500 MeV $Ne^{10+} \rightarrow U$.

The electron capture from the target L shell into the projectile K shell and the contribution of intrashell coupling to the ionization probabilities have been taken into account. Their partial cancellation resulted in a net effect that in most cases is of the order of the experimental uncertainties.

In conclusion, despite the complexity of the heavy ion induced spectra, the proper choice of the colliding systems and a suitable approach in the analysis allows us to be decisive on the validity of theoretical approximations concerning electron ionization. Our achieved results concerning the L (sub)shell opens the possibility to extrapolate to the higher atomic shells.

ACKNOWLEDGMENTS

The authors are particularly indebted to Professor O. W. Schult for valuable discussions, and for encouraging and supporting this work. We would like to thank the staff of the Jülich and KVI cyclotrons for their efficient cooperation during the beam time experiments. We enjoyed the collaboration with Professor J.-Cl. Dousse and his group from the University of Fribourg, and with Professor Z. Sujkowski and his group from SIN, Swierk during the measurements at KVI. We appreciated many fruitful discussions with Professor D. Trautmann and Dr. Z. Halabuka, University of Basel, and Professor B. Fricke, University of Kassel, concerning the interpretation of the data.

[1] Proceedings of the Sixth International Conference on PIXE and Its Analytical Applications, Tokyo, Japan, 1992, edited by M. Uda [Nucl. Instrum. Methods Phys. Res. B **75**, (1993)].

[2] Proceedings of the Seventh International Conference on PIXE and Its Analytical Applications, Padua, Italy, 1995, edited by G. Moschini and V. Valkovic [Nucl. Instrum. Methods Phys. Res. B **109/110**, (1996)].

[3] V. P. Petukhov, I. Török, and M. Terasawa, Nucl. Instrum. Methods Phys. Res. B **109/110**, 105 (1996), and references therein.

[4] P. Tesauro, P. A. Mandò, G. Parrini, A. Pecchioli, and P. Sona, Nucl. Instrum. Methods Phys. Res. B **108**, 197 (1996).

[5] M. G. Budnar, Nucl. Instrum. Methods Phys. Res. B **109/110**, 144 (1996).

[6] F. Folkmann, Nucl. Instrum. Methods Phys. Res. B **75**, 9 (1993).

[7] M. Mochizuki, T. Yamamoto, S. Nagashima, and M. Uda, Nucl. Instrum. Methods Phys. Res. B **109/110**, 31 (1996).

[8] B. Perny, J.-Cl. Dousse, M. Gasser, J. Kern, Ch. Rheme, P. Rymuza, and Z. Sujkowski, Phys. Rev. A **36**, 2120 (1987).

[9] M. Carlen, J.-Cl. Dousse, M. Gasser, J. Kern, Ch. Rheme, P. Rymuza, Z. Sujkowski, and D. Trautmann, Europhys. Lett. **13**, 231 (1990).

[10] P. Rymuza, T. Ludziejewski, Z. Sujkowski, M. Carlen, J.-Cl. Dousse, M. Gasser, J. Kern, and Ch. Rhême, Z. Phys. D **23**, 81 (1992).

[11] M. Carlen, J.-Cl. Dousse, M. Gasser, J. Hoszowska, J. Kern, Ch. Rhême, P. Rymuza, Z. Sujkowski, and D. Trautmann, Z. Phys. D **23**, 71 (1992).

[12] M. W. Carlen, B. Boschung, J.-Cl. Dousse, Z. Halabuka, J. Hoszowska, J. Kern, and Ch. Rhême, Phys. Rev. A **49**, 2524 (1994).

[13] R. Salziger, G. L. Borchert, D. Gotta, O. W. B. Schult, D. H. Jakubassa-Amundsen, P. A. Amundsen, and K. Rashid, J. Phys. B **22**, 821 (1989).

[14] D. F. Anagnostopoulos, G. L. Borchert, D. Gotta, and K. Rashid, Z. Phys. D **18**, 139 (1991).

[15] D. F. Anagnostopoulos, G. L. Borchert, and D. Gotta, J. Phys. B **25**, 2771 (1992).

[16] T. Ludziejewski, J. Hoszowska, P. Rymuza, Z. Sujkowski, D. Anagnostopoulos, G. Borchert, M. Carlen, J.-Cl. Dousse, Ch. Rhême, and A. G. Drentje, Nucl. Instrum. Methods Phys. Res. B **63**, 494 (1992).

[17] G. L. Borchert, J. Bojowald, A. Ercan, H. Labus, Th. Rose, and O. W. B. Schult, Nucl. Instrum. Methods Phys. Res. A **245**, 393 (1986).

[18] M. A. Blokhin, in *Advances in X-Ray Spectroscopy*, edited by C. Bonnelle and C. Mandé (Pergamon, Oxford, 1982), 90–103; B. K. Agarwal, *X-ray Spectroscopy* (Springer-Verlag, Berlin, 1991), p. 314.

[19] S. I. Salem and P. L. Lee, At. Data Nucl. Data Tables **18**, 233 (1976).

[20] M. O. Krause and J. H. Oliver, J. Phys. Chem. Ref. Data **8**, 329 (1979); M. O. Krause, *ibid.* **8**, 307 (1979).
[21] J. A. Bearden, Rev. Mod. Phys. **39**, 78 (1967).
[22] J. P. Desclaux, Comput. Phys. Commun. **9**, 31 (1975).
[23] D. F. Anagnostopoulos, Forschungszentrum Jülich GmhH, Report No. 2667, ISSN 0366-0885 (1992).
[24] J. Bang and J. M. Hansteen, Mat. Fys. Medd. K. Dan. Vidensk. Selsk. **31**, No 13 (1959).
[25] K. Ashamar and P. A. Amundsen, J. Phys. B **14**, 483 (1981).
[26] D. Trautmann and F. Rösel, Nucl. Instrum. Methods **169**, 259 (1980).
[27] P. A. Amundsen, J. Phys. B **11**, 3197 (1978).
[28] K. Ashamar, T. M. Luke, and J. D. Talman, At. Data Nucl. Data Tables **22**, 443 (1978).
[29] K. Ashamar and P. A. Amundsen, J. Phys. B **21**, 2709 (1988).
[30] S. T. Perkins, D. E. Cullen, M. H. Chen, J. H. Hubbell, J. Rathkopf, and J. Scofield, *Tables and Graphs of Atomic Subshell and Relaxation Data Derived from the LLNL Evaluated Atomic Data Library (EADL), Z=1–100* (Lawrence Livermore National Laboratory, Livermore, CA, 1991), Vol. 30.
[31] J. M. Hansteen, O. M. Johnsen, and L. Kocbach, At. Data Nucl. Data Tables **15**, 305 (1975).
[32] L. Sarkadi and T. Mukoyama, J. Phys. B **14**, L255 (1981).
[33] P. A. Amundsen and D. H. Jakubassa-Amundsen, J. Phys. B **21**, L99 (1988).
[34] G. Mehler, J. Reinhardt, B. Müller, G. Greiner, and G. Soff, Z. Phys. D **5**, 143 (1987).
[35] K. Desheimer, Ullrich, K. E. Stibing, W. Schadt, S. Kelbch, C. Kelbch, R. Schuch, S. Zehender, and H. Schmidt-Böcking, J. Phys. B **19**, 3083 (1986).
[36] I. C. Legrand, V. Zoran, P. Dorner, H. Schmidt, Bocking, A. Berinde, D. Fluerasen, and C. Ciortea, J. Phys. B **25**, 189 (1992).
[37] J. H. Macek and R. Shakeshaft, Phys. Rev. A **22**, 1441 (1980).
[38] D. H. Jakubassa-Amundsen and P. A. Amundsen, Z. Phys. A **297**, 203 (1980).
[39] D. H. Jakubassa-Amundsen, Z. Phys. A **316**, 161 (1984).
[40] H. Ogawa (private communication); I. Katayama, H. Ikegami, H. Ogawa, Y. Haruyama, M. Tozaki, A. Aoki, F. Fukuzawa, K. Yoshida, and I. Sugai, Phys. Rev. A **53**, 242 (1996).
[41] J. M. Hansteen and O. P. Mosebekk, Phys. Rev. Lett. **29**, 1361 (1972).
[42] J. H. McGuire and L. Weaver, Phys. Rev. A **16**, 41 (1977).
[43] M. Polasik, Phys. Rev. A **39**, 616 (1989).
[44] D. F. Anagnostopoulos, J. Phys. B **28**, 47 (1995).
[45] J. H. Hubbell, P. N. Trehan, N. Singh, B. Chand, D. Mehta, M. L. Garg, R. R. Garg, S. Singh, and S. Puri, J. Phys. Chem. Ref. Data **23**, 339 (1994).
[46] M. Polasik, Phys. Rev. A **39**, 5092 (1989); **40**, 4361 (1989); **41**, 3689 (1990).
[47] P. Rymuza, Z. Sujkowski, M. Carlen, J.-Cl. Doussee, M. Gasser, J. Kern, B. Perny, and Ch. Rhême, Z. Phys. D **14**, 37 (1989).